



**HAL**  
open science

# Optical properties of cometary particles collected by the COSIMA mass spectrometer on-board Rosetta during the rendezvous phase around comet **67P/Churyumov–Gerasimenko**

Yves Langevin, Martin Hilchenbach, Matthieu Vincendon, Sihane Merouane,  
K. Hornung, Nicolas Ligier, C. Engrand, R. Schulz, J S Kissel, J. Rynö

## ► To cite this version:

Yves Langevin, Martin Hilchenbach, Matthieu Vincendon, Sihane Merouane, K. Hornung, et al.. Optical properties of cometary particles collected by the COSIMA mass spectrometer on-board Rosetta during the rendezvous phase around comet 67P/Churyumov–Gerasimenko. Monthly Notices of the Royal Astronomical Society, 2017, 469 (Suppl\_2), pp.S535-S549. 10.1093/mnras/stx2070 . insu-02985964

**HAL Id: insu-02985964**

**<https://insu.hal.science/insu-02985964>**

Submitted on 2 Nov 2020

**HAL** is a multi-disciplinary open access archive for the deposit and dissemination of scientific research documents, whether they are published or not. The documents may come from teaching and research institutions in France or abroad, or from public or private research centers.

L'archive ouverte pluridisciplinaire **HAL**, est destinée au dépôt et à la diffusion de documents scientifiques de niveau recherche, publiés ou non, émanant des établissements d'enseignement et de recherche français ou étrangers, des laboratoires publics ou privés.

# Optical properties of cometary particles collected by the COSIMA mass spectrometer on-board *Rosetta* during the rendezvous phase around comet 67P/Churyumov–Gerasimenko

Y. Langevin,<sup>1★</sup> M. Hilchenbach,<sup>2★</sup> M. Vincendon,<sup>1</sup> S. Merouane,<sup>2</sup> K. Hornung,<sup>3</sup> N. Ligier,<sup>4</sup> C. Engrand,<sup>5</sup> R. Schulz,<sup>6</sup> J. Kissel,<sup>2</sup> J. Rynö<sup>7</sup> and the COSIMA team

<sup>1</sup>*Institut d'Astrophysique Spatiale, CNRS/Univ. Paris-Sud, F-91405 Orsay, France*

<sup>2</sup>*Max-Planck Institut für Sonnensystemforschung, D-37077 Göttingen, Germany*

<sup>3</sup>*Universität der Bundeswehr, LRT-7, D-85577 Neubiberg, Germany*

<sup>4</sup>*Open University, Milton Keynes, MK7 6BJ, UK*

<sup>5</sup>*CSNSM, CNRS/Univ. Paris-Sud, F-91405 Orsay, France*

<sup>6</sup>*European Space Agency Scientific Support Office, NL-2201 AZ Noordwijk, the Netherlands*

<sup>7</sup>*Finnish Meteorological Institute, FI-00101 Helsinki, Finland*

Accepted 2017 August 9. Received 2017 August 7; in original form 2017 April 21

## ABSTRACT

40 000 collected cometary particles have been identified on the 21 targets exposed by the COSIMA experiment on-board *Rosetta* to the environment of comet 67P/Churyumov–Gerasimenko from 2014 August to 2016 September. The images of the targets were obtained by the COSIMA microscope (Cosiscope,  $13.95 \mu\text{m pixel}^{-1}$ ) with near grazing incidence, which is optimal for the primary objective (detection of collected particles) but very challenging for photometry. However, more than 300 of the collected particles are larger than  $100 \mu\text{m}$  which makes it possible to derive constraints on the optical properties from the distribution of light levels within the particles. Two types of particles collected by COSIMA (compact particles and cluster particles) have been identified in Langevin et al. The best estimate reflectance factors of compact particles range from 10 per cent to 23 per cent. For cluster particles (>90 per cent of large collected particles), the comparison of the signal profiles with illumination from two opposite directions shows that there is scattering within the particles, with a mean free path in the 20–25  $\mu\text{m}$  range, which requires high porosity. The best estimate reflectance factors of cluster particles range from 3 per cent to 22 per cent. This range of reflectance factors overlaps with that obtained from observations of the cometary nucleus at macroscopic scales by OSIRIS and it is consistent with that measured for interplanetary dust particles collected in the stratosphere of the Earth.

**Key words:** comets: general – planets and satellites: formation.

## 1 INTRODUCTION

COSIMA is a time-of-flight secondary ion mass spectrometer on-board the *Rosetta* orbiter dedicated to analysing dust particles collected close to comet 67P/Churyumov–Gerasimenko (Kissel et al. 2007). The primary beam is provided by an indium source with a limited supply. The particles are collected on targets  $10 \text{ mm} \times$

$10 \text{ mm}$  in size. A microscope (Cosiscope) was included in the design of COSIMA, imaging exposed targets before and after each exposure so as to detect collected cometary particles.

Given the range of pre-encounter dust models, the COSIMA team had to consider the possibility that only a few 10s small particles would be identified after a week-long exposure during the first months of the rendezvous phase. The major design driver for Cosiscope was therefore to achieve the highest possible detection probability for small collected particles. This led to the selection of a near grazing incidence with two opposite light directions, as such a configuration drastically enhances the signal of a particle sticking out of a target.

\* E-mail: [yves.langevin@ias.u-psud.fr](mailto:yves.langevin@ias.u-psud.fr) (YL); [hilchenbach@mps.mpg.de](mailto:hilchenbach@mps.mpg.de) (MH)

This detection scheme led to the identification of more than 100 particles identified during the first month of the rendezvous phase, when the distance of *Rosetta* to the nucleus was 50 km or more, at a distance of 3.4 au from the Sun. More than 2600 particles were identified until early 2014 December, most being collected when the comet was farther than 3 au from the sun. At the end of the orbital phase (2016 September 29), more than 40 000 cometary particles have been identified, many resulting from the fragmentation of large parent particles during collection (Merouane et al. 2016). The primary goal of Cosiscope, i.e. identifying the locations of cometary particles for mass spectrometry analysis, has therefore been achieved.

Many collected particles extend over areas larger than the ion beam size ( $\sim 100 \mu\text{m}$ ), which proved quite useful for obtaining information on the composition of cometary material after handling a target contamination issue (see e.g. Fray et al. 2016; Hilchenbach et al. 2016). The unexpected number of large collected particles results from a distribution in size which turned out to be ‘flatter’ than expectations, with an integral power index of  $-1$  for particles  $< 1 \text{ mm}$  from GIADA (Rotundi et al. 2015) and  $-0.8 \pm 0.1$  for particles from  $150 \mu\text{m}$  to  $1 \text{ mm}$  from Cosiscope (Merouane et al. 2016). For particles with sizes smaller than  $150 \mu\text{m}$ , the distribution is steeper ( $-1.9 \pm 0.3$ ), in line with the flattest pre-encounter estimates (Fulle et al. 2010).

The collection of many particles more than 5 pixels across (pixel size:  $14 \mu\text{m}$ , see Section 2) made it possible to reveal a diverse typology, with two categories of collected particles, compact particles and cluster particles (Langevin et al. 2016). Compact particles have retained their shape upon collection, contrary to cluster particles, due to a larger tensile strength (Hornung et al. 2016). Among cluster particles, ‘glued clusters’, ‘rubble piles’ and ‘shattered clusters’ have been identified on the basis of the increasing spread between cluster components. Compact particles exhibit a complex sub-structure down to the resolution of Cosiscope ( $\sim 10 \mu\text{m}$  with sub-pixel sampling) and no good candidate for a large monocrystalline particle has been identified. Therefore, all the particles collected by COSIMA are likely to be aggregates, in line with observations of micrometeorites or interplanetary dust particles collected in the stratosphere of the Earth.

In this contribution, we report results on the optical properties of the collected particles. This is a challenge as the near grazing incidence that was selected for optimum detection results in light levels for each pixel which are controlled by geometry as much or more than by the intrinsic photometric properties of the particles. Furthermore, the phase angle is always close to  $80^\circ$ ; hence, one cannot constrain scattering properties from phase functions. For aggregate particles, the reflectance factor (fraction of the light scattered back by a surface assuming Lambert scattering, closely related to the geometric albedo) has to be considered with caution, in the framework of multiple scattering models with distances between interactions much larger than the wavelength.

In Section 2, the photometric characteristics of Cosiscope will be discussed, so as to derive a reliable distribution of light levels across the collecting targets. In Section 3, the approach selected for constraining the reflectance factor of cometary particles under near grazing incidence will be presented, taking into account the possible role of scattering within the particles due to porosity. The results on the optical properties of collected particles larger than  $\sim 100 \mu\text{m}$  and the time evolution of these optical properties during the rendezvous phase will be presented in Section 4.

## 2 CHARACTERISTICS OF COSISCOPE AND OF THE COSIMA TARGETS RELEVANT FOR PHOTOMETRY

### 2.1 Targets, imaging device and imaging procedures

The targets for the flight model of COSIMA are silver squares  $10 \text{ mm} \times 10 \text{ mm}$  covered with several types of target coatings, from very smooth, thin coatings (‘gold black’  $8 \mu\text{m}$  to  $30 \mu\text{m}$  thick, Hornung et al. 2014) to very rough coatings. ‘Gold black’ targets were best suited for optical detection of particles sticking out of the gold black layer while rougher targets were expected to provide improved collection efficiencies and would have been considered if the first collection attempts had proven unsuccessful. The different types of targets had been distributed over the 24 available target assemblies. The first target assembly, D0, was exposed from 2014 August to 2014 December (first 4.5 months of the orbital phase).  $\sim 2600$  collected particles were optically detected on the three gold black coated targets. When selecting the six target assemblies exposed later in the mission (CF, C7, D1, CD, D2 and C3 in chronological order), those with gold black targets were preferentially selected, so that 17 of the 21 exposed targets (including the three targets of D0) had a gold black coating. Two ‘silver blank’ targets with no coating (1C7 and 1D1) and two ‘silver black’ targets (2C7 and 3D2) were also exposed. Silver black targets are similar to gold black targets with a  $10\text{--}30 \mu\text{m}$  deposit of silver instead of gold on to the silver base plate. Both types of targets show structure on a scale of  $< 30 \mu\text{m}$ , but they appear homogeneous at larger scales. The reflectance factor of silver black and gold black was evaluated in the laboratory with respect to a reference (WS-1 from Ocean optics) with a reflectance factor of 98 per cent at  $640 \text{ nm}$  at an incidence of  $20^\circ$ . As the emergence is close to  $0^\circ$ , both the reference, which is relatively smooth, and the metal black targets, which are rough at a very small scale, can be expected to follow a Lambert scattering law for a wide range of incidences (up to more than  $80^\circ$  for the Cosiscope images). While both are quite dark, silver black (reflectance factor of  $11 \pm 1$  per cent at large scales) is brighter than gold black ( $1.8 \pm 0.6$  per cent). ‘Silver blank’ targets have no coating; hence, specular reflection plays a major role and Lambert scattering does not apply.

The imaging set-up of COSIMA has been presented in Kissel et al. (2007) and Langevin et al. (2016). The microscope is a 1:1 imaging system projecting a  $14.2 \times 14.2 \text{ mm}$  area on to a TH7888 CDD detector ( $1024 \times 1024$  pixels, each  $13.9 \mu\text{m} \times 13.9 \mu\text{m}$  in size). For imaging, each of the three targets of a target assembly is positioned by the target manipulating unit (TMU) between two red LED’s ( $\lambda = 640 \text{ nm}$ ) set  $2 \text{ mm}$  above the focal plane  $10 \text{ mm}$  to the right and  $6 \text{ mm}$  to the left of the edge of the  $10 \text{ mm} \times 10 \text{ mm}$  target (Fig. 1). The incidence ranges from  $78.7^\circ$  to  $84.3^\circ$  for LED P and from  $71.7^\circ$  to  $82.9^\circ$  for LED M.

The three targets of each target assembly are imaged in succession (1, then 2, then 3) by moving the target assembly twice by  $11 \text{ mm}$  in the  $+Y$  direction with the TMU. For each target, two images are obtained after switching on LED P alone, then LED M alone. The first images were obtained with an exposure time of  $300 \text{ ms}$ . An exposure time of  $200 \text{ ms}$  was used after 2014 December so as to avoid near saturation of bright particles close to the LED. Signal levels have been scaled to  $200 \text{ ms}$  when a different exposure time was used.

A reliable procedure was defined for moving the target assembly by close to half a pixel ( $6.95 \mu\text{m}$ ). This made it possible to obtain sub-sampled sets of four images with positions in a square

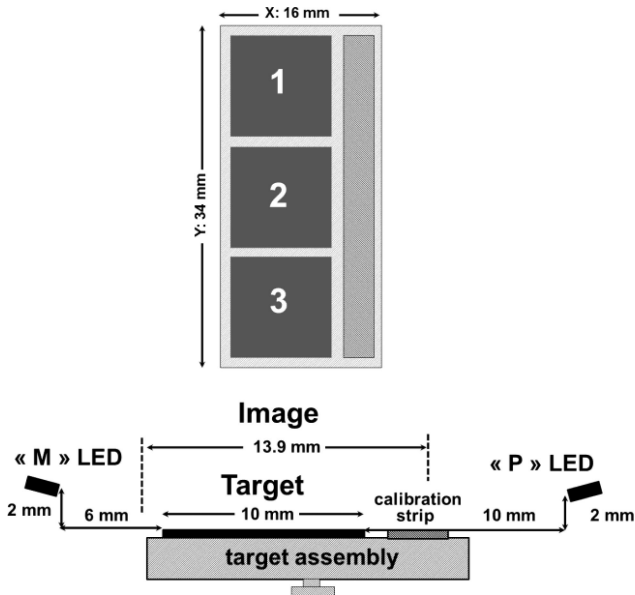


**Figure 1.** Optical configuration for observing collected particles with Cosiscope. The target names correspond to their position followed by the target assembly name (1D0 for target in position ‘1’ of target assembly ‘D0’). The name of a collected particle associates the target on which it was collected with a given name (e.g. ‘3D0/Nick’).

6.95  $\mu\text{m} \times 6.95 \mu\text{m}$  in size. Sub-pixel sampling improves the spatial resolution, with an upper limit of  $\sim 10 \mu\text{m}$  for the equivalent sampling interval. It also improves pixel statistics for particles by a factor of 4. Therefore, the evaluation of optical properties of collected particles has been made from sub-sampled images, with the exception of the last target assembly, for which sub-pixel sampling could not be implemented after the end of exposure due to the collision with the nucleus.

## 2.2 Distribution of light levels on ‘gold black’ targets at all three positions on the target assembly

Obtaining constraints on the reflectance properties of collected particles requires determining the illumination conditions for the region of the target where they have been collected. Light from the LEDs is spread as a broad conical fan through a small lens  $\sim 1 \text{ mm}$  in diameter. The illumination decreases away from the boresight in a pattern that is specific to each LED, reaching an angular distance of more than  $40^\circ$  as the nearest edge of the target (10 mm across) can be imaged 6 mm away from LED M. The incidence increases with the distance to the LED (from 6 mm at the near edge for LED M up to 20.4 mm for the lower far edge from LED P). The cosine of this incidence is close to  $2/D$  (where  $D$  is the distance in mm), so that when the variations in incidence are combined with the decrease in flux within each element of solid angle ( $1/D^2$ ), the light level on the target is expected to decrease rapidly with distance from the LED, as  $1/D^3$ . Once positioned for imaging, all targets share the same relationship with the light source (LED P or LED M); hence, the light distribution from the LED should be the same.

As can be seen from Figs 2(c)–(f), the gradients differ very significantly in most cases from a dependence as  $1/D^3$ . More surprisingly, the light patterns are quite specific to each target position (‘1’, ‘2’ or ‘3’ in Fig. 1) as demonstrated by the quite different light profiles of Figs 2(c) and (d) (LED P and LED M, target 3C7, in position

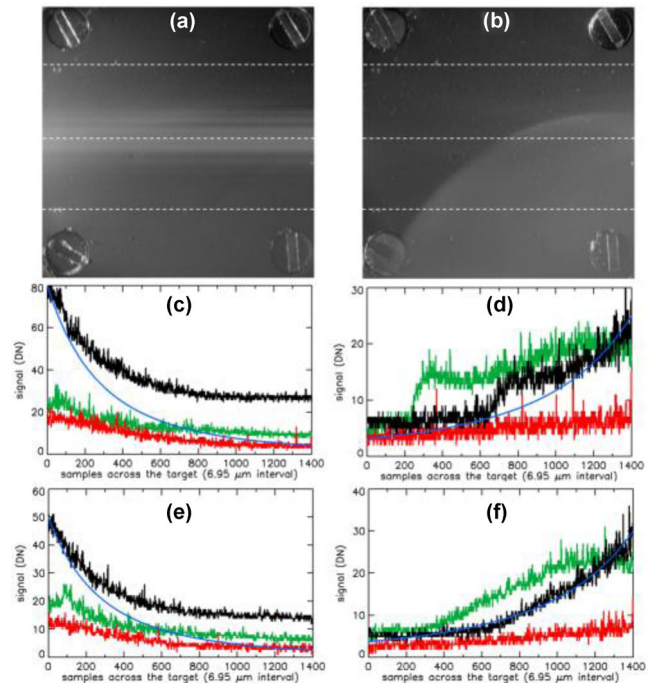


**Figure 2.** Images and profiles across gold black targets obtained before collection. (a) Image of target 3C7 obtained with LED M, displayed with a log scale for clarity as the target is very dark. A spill-over electronic contribution from saturated parts of the image left of the target is observed for the lines halfway up the target. (b) Image of target 3C7 with LED P (log scale). A stray light contribution can be observed in an area with a circular boundary at bottom right. (c) Signal with LED M along the central line of target 3C7 (black) and two lines in the lower part of the target (green) and the higher part of the target (red). The blue line corresponds to a decrease as  $1/D^3$ . (d) Signal with LED P for target 3C7 along the same lines. (e) Profiles with LED M for target 1D2. (f) Profiles with LED P for target 1D2.

‘3’) compared to Figs 2(e) and (f) (LED P and LED M, target 1D2, in position ‘1’). These discrepancies result from two artefacts that need to be corrected as they impact the light profile at levels of 5–20 digital numbers (DN), similar to the low signal from dark targets: an electronic spill-over with LED M, and a stray light contribution that has a different pattern for each LED and for each target position.

### 2.2.1 Electronic spill-over with LED M

The region of the target assembly which is imaged to the left of the target (Figs 1 and 4a) is located 5–6 mm away from LED M, which leads to highly saturated signals close to the centre line. As the lines are read from left to right, this generates additional electrons as a spill-over, which remains the same across the image as demonstrated by Fig. 2(a). A correction to be applied to the full image can be obtained with an estimated accuracy of  $\pm 5$  per cent by taking as a reference a column at the right edge of the image (over the calibration strip) and by fitting regions free of electronic spill-over with a polynomial (Fig. 3) so as to evaluate the spill-over contribution. The reflectivity of the target assembly left of the target is specific to each target; hence, this correction ranges from up to 8.5 DN for target 1D2 (Fig. 3) to more than 20 DN close to the centre line of target 3C7 (Fig. 2c). An example of correction with actual particles is provided for the LED M image of target 3D0 after collection (Fig. 4). The particles themselves do not show any change after correction (Fig. 4b), as the signal reaches several 100

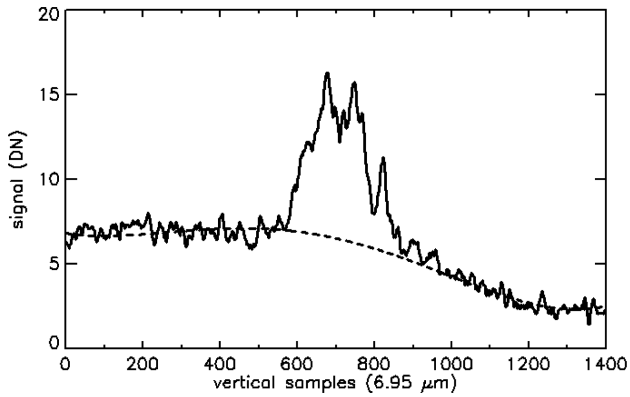


**Figure 3.** Vertical profile across target 1D2 close to the right edge of a gold black target as observed with LED M. The dashed line corresponds to a fifth-order polynomial fit of the regions from line 0 to 600 and 1000 to 1400 for which the contribution of the electronic spill-over is small.

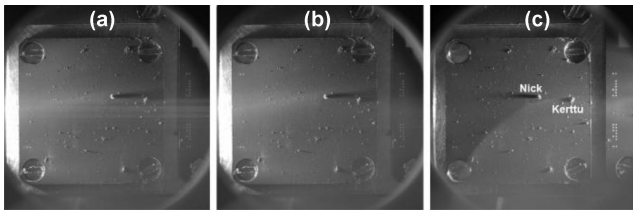


**Figure 4.** Image of target 3D0 with LED M in log scale at the end of the collection period without correcting for the electronic spill-over (a) and after correction with a single profile subtracted to each column (b); (c) image of 3D0 in log scale with LED P.

DN, but the gold black target has a more regular light profile and the contrast of shadows is much improved in the central horizontal strip.

After correction, the image quality with LED M (Fig. 4b) becomes similar to that with LED P (Fig. 4c). As can be seen in Fig. 4(c), the right edge of the image is occupied by the calibration strip (see Fig. 1), which is covered with gold black; hence, it does not saturate when LED P is switched on and there is no electronic glare similar to that observed with LED M.

### 2.2.2 Stray light contribution

An additional contribution is most prominent at bottom right with LED P for targets in the ‘3’ positions (Figs 2b and d). This contribution scales with the integration time; hence, it corresponds to an actual signal.

The first major clue comes from the observation of shadows of the two largest particles on target 3D0, 3D0/Nick and 3D0/Kerttu. As shown in Fig. 5(c), one of these two particles (3D0/Kerttu) lies inside and the other (3D0/Nick) outside the region exhibiting a spurious signal. Both exhibit a flat umbra (no photons coming directly from LED P). The signal levels for Nick are  $\sim 3$  DN in the umbra and  $\sim 19$  DN out of the shadow (Fig. 5a). For 3D0/Kerttu, the contrast of the shadow is much weaker (12 DN/32 DN, Fig. 5c). A secondary source of additional photons coming from LED P after one or several specular reflections can be ruled out as at a level of 12 DN (Kerttu), a secondary shadow would then be readily identified in the direction opposite to the source on an image in log scale, which is not the case (Fig. 5d). There is evidence for a non-directional contribution generating a weak ‘particle shine’ on the back-side of

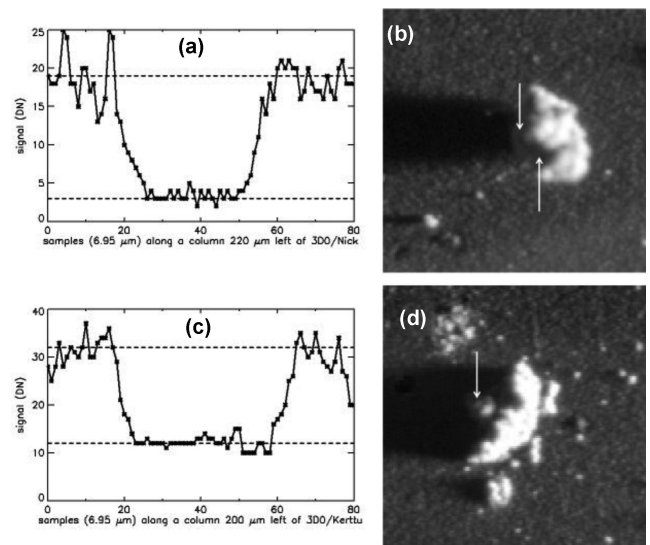


**Figure 5.** Shadows of large compact particles with LED P on target 3D0; (a) vertical profile across the shadow of 3D0/Nick. A constant level of  $\sim 3$  DN is observed over  $170 \mu\text{m}$ . (b) Image of 3D0/Nick with LED P on a log scale. The backsides of the particles are weakly illuminated (arrows) by photons not coming directly from LED P. (c) Vertical profile across the shadow of 3D0/Kerttu. The central area is flat, but at a higher level (12 DN) than for 3D0/Nick; (d) image of 3D0/Kerttu with LED P on a log scale.

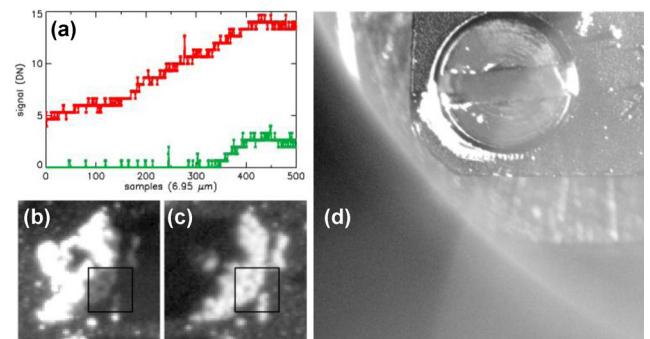


**Figure 6.** Clues for the origin of the additional contribution for LED P; (a) horizontal signal profiles for the top left corner (green) and for the bottom left corner (red) of target 3D0 with LED P; (b) image of 3D0/Kerttu with LED M (log scale), with all directly lit areas set to a constant value for bringing out details in the shadow; (c) image of 3D0/Kerttu with LED P; (d) lower left corner of the image of target 3D0 (log scale).

Nick with LED P ( $\sim 13$  DN, Fig. 5b) or Kerttu (Fig. 6b) where a structured part of the particle in the shadow is definitely imaged as the pattern matches that observed with LED P (Fig. 6c). However, these ‘particle shines’ are extremely weak, with factors of 40–50 compared to the front side of the particle. When considering the low reflectance factor of gold black (1.8 per cent), this non-directional contribution can only reduce the contrast of the shadow by a small fraction of a DN.

The only remaining hypothesis for the additional contribution is that it results from stray light going directly from the LED to the interior of the camera casing (then to the detector) without interacting with the target. This is supported by Fig. 6(d), which shows the boundary of the region with enhanced signal crossing beyond the limits of the field of view on a LED P image of target 3D0. This conclusion is confirmed by the analysis of images of a target covered with silver black (3D2) at the same position (‘3’)

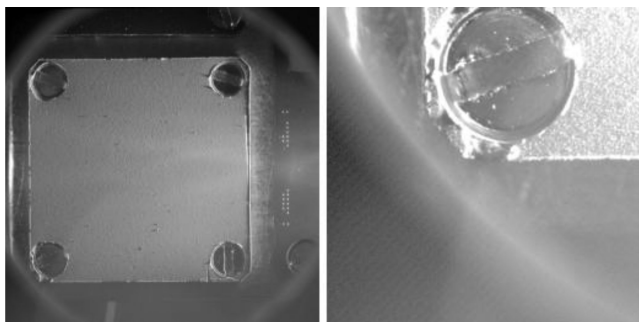


**Figure 7.** Image of target 3D2 (silver black) before collection with LED P in log scale; left: full image, which shows that 3D2 is homogeneous at medium to large scales; right: lower left corner, rescaled to the same dynamics as Fig. 6(d), which brings up the additional contribution extending out of the FOV, with a pattern very similar to that on the image of 3D0.

as 3D0. Its reflectance factor is  $\sim 6$  times larger than that of gold black from laboratory measurements. The contrast of the additional contribution is now much weaker (Fig. 7a), and it can only be observed (Fig. 7b) when rescaling the image to the same dynamics as Fig. 6(d). This provided a method for evaluating the stray light contribution by assuming that it was constant for each target position, independently of the reflectance factor of the target.

The determination of the stray light pattern and legitimate light pattern from the LEDs across the targets involved the following steps:

- 1) Subtraction of the electronic spill-over for the images with LED M.
- 2) Derivation of median averaged images before collection for a silver black target (3D2) and a gold black target (3D0). This procedure eliminates the small-scale roughness that is larger for silver black (3D2) than for gold black (3D0), as well as small particles sticking out of the metal layer before collection.
- 3) Subtraction of the median averaged 3D0 image (gold black) from the median averaged 3D2 image (silver black, higher reflectance factor). The stray light having been subtracted out, the resulting signal should be proportional to the difference in reflectance factor between silver black and gold black; hence, it constitutes a reliable evaluation of the actual distribution of light reaching the target.

As shown by Fig. 8, this approach is quite successful for LED P and LED M: A single light profile (blue for 3D2, scaled to green for 3D0) matches quite well the signal (dashed black lines) after subtracting the same stray light contribution (red lines). The ratio between silver black and gold black is  $\sim 6.8$  for LED P,  $\sim 5.6$  for LED M, both close to the expected ratio ( $11/1.8 = 6.1$ ). The small discrepancy can be attributed to a slightly more favourable tilt (by  $0.75^\circ$ ) of 3D2 with respect to LED P, which becomes slightly unfavourable with respect to LED M. The stray light level reaches 13 DN in the lower part of the target for LED P and  $\sim 6$  DN for LED M (both with an exposure time of 200 ms).

Comparing the silver black target (3D2) with other gold black targets in position 3 (e.g. 3C7) leads to a very similar outcome in terms of both the light intensity pattern and the stray light pattern, which confirms the validity of this approach.

The resulting generic patterns for light intensities on homogeneous surfaces are presented in Fig. 9. These generic light intensity patterns are realistic for relatively smooth light fans with a stronger light beam up of centre for LED M and weaker privileged directions

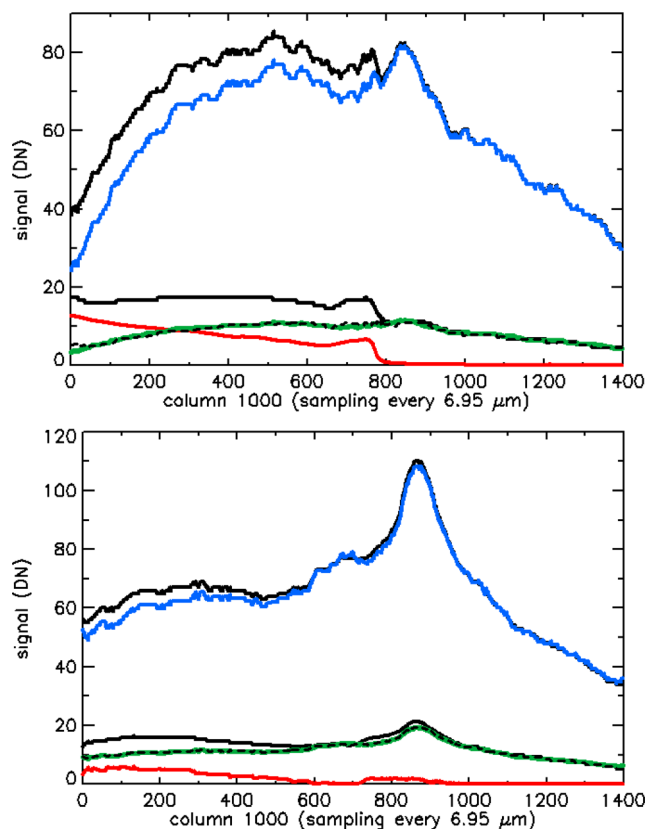


**Figure 8.** Correction method applied to column 1000 (near the centre of the image) for LED P (top panel) and LED M (bottom panel), after subtracting the electronic spill-over contribution; upper black solid line: raw signal from 3D2; lower black solid line: raw signal from 3D0; blue solid line: profile of the light reaching the target as determined from the difference of raw signals from 3D2 and 3D0, scaled so as to match the upper part of the 3D2 profile; green solid line: the same light profile scaled so as to match the upper part of the 3D0 profile; red solid lines: stray light contribution (the same for 3D2 and 3D0); dashed black lines: signal – stray light for 3D0.

for LED P. They provide the reference for evaluating the reflectance properties of collected particles for each location on the target.

The outcome of the stray light correction (Fig. 10, right) is visually convincing as the spurious circular boundary has been removed. The high contrast of shadows of particles collected on 3D0 (position ‘3’) in the region most impacted by stray light also support the validity of the stray light correction approach.

This confirms the conclusions from the very low level of ‘particle shine’: At least 97.5 per cent of the photons reaching the target (or collected particles) come directly from the LED, with a grazing incidence for the reference target (3D2, reflectance factor 11 per cent) which is well-defined within the limits set by the size of the exit lens of the LEDs.

The generic light pattern for photons reaching a target in position 3 which has been obtained from comparing silver black (3D2) and gold black (3D0, 3C7...) can be applied to the two other target positions as the targets themselves are in the same position relative to the LEDs. Similarly to target position ‘3’, the signal level in the shadows of large particles on targets in position ‘1’ and ‘2’ is only a few DN after subtracting the relevant stray light pattern, which validates the stray light correction procedure for these positions.

Small tilts ( $< 1^\circ$ ) towards or away from the LED have only a minor impact when evaluating the reflectance properties of collected particles as they stick out of the gold black layer, with local slopes

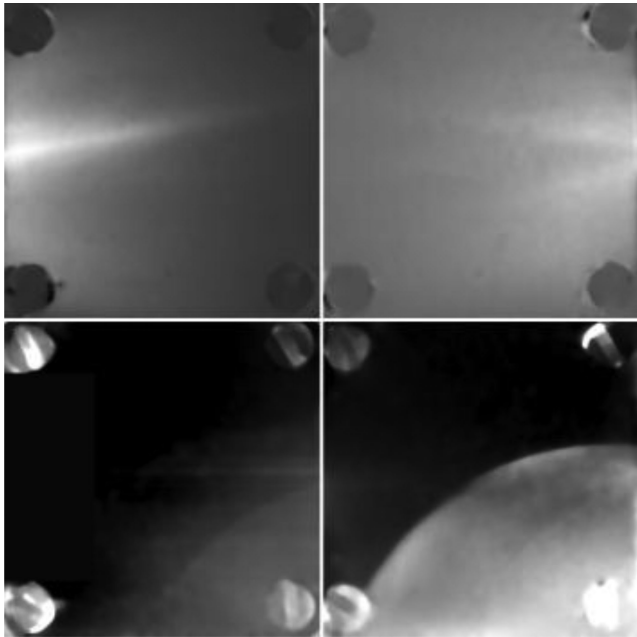


**Figure 9.** Best estimate on the generic light pattern on a uniform target for LED M (top left) and LED P (top right) with a linear grey scale; stray light distribution for targets in position ‘3’ with LED M (bottom left) and LED P (bottom right) with a grey scale from 0 to 15 DN. The derivation method is not relevant for screws.

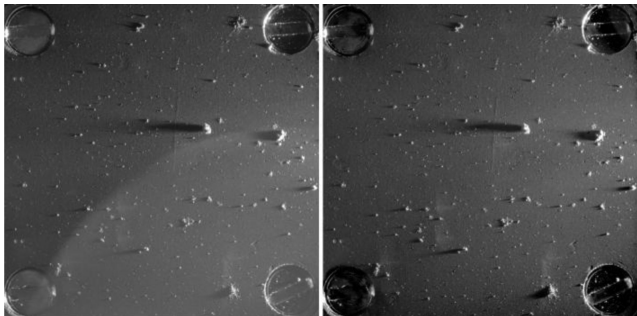


**Figure 10.** Image of target 3D0 with LED P (log scale) before (left) and after (right) subtracting the stray light contribution.

in the 20–90° range. The relevant parameter is the local incidence compared to that of the reference target (3D2), not the collecting target, and a single reference for the light pattern can be applied in all cases. The only two targets for which generic light patterns (P and M) are not representative are the two ‘silver blank’ targets, 1C7 and 1D1, as specular reflection can nearly double the light level reaching the front side of a particle. Therefore, particles collected on these two targets have not been considered for the determination of optical properties.

### 3 EVALUATING REFLECTANCE PROPERTIES OF COLLECTED PARTICLES WITH COSISCOPE

#### 3.1 The surface scattering assumption and its limitations

The presence of well-defined, high-contrast shadows for all large particles led to test as a first step the assumption that photon scattering occurs at the very surface (within a few wavelengths with physical optics). As all collected particles show substructure down

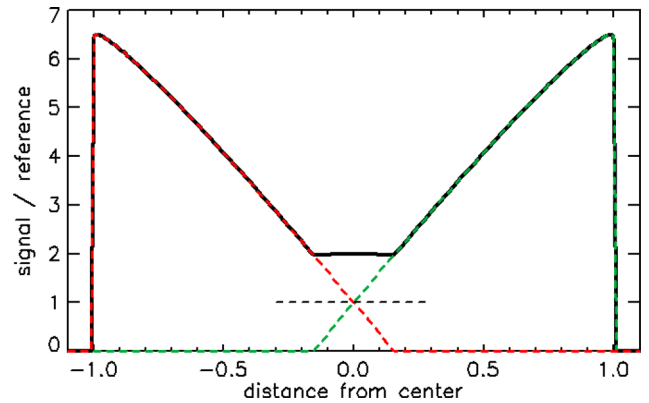


**Figure 11.** Expected profiles along the X axis (M–P direction) of the signal/reference ratio for a spherical particle with a reflectance factor of 11 per cent equal to that of the reference silver black target ( $R_r = 1$ ) 13 mm away from both LEDs; red dashed line: LED P; green dashed line: LED M; black solid line: sum of the two profiles. At crossover, the signal/reference ratio is 1 for both LEDs.

to the resolution of Cosiscope, they are expected to exhibit significant surface roughness at scales much smaller than the size of the particle, with scattering properties following Lambert’s law (radiance proportional to the cosine of emergence).

The highest region of any particle has a convex shape (otherwise it would not contain the highest point). The radius of curvature is larger for a dome-like profile than for a sharp edge. If this radius of curvature is at least as large as the pixel size (13.9  $\mu\text{m}$ ), the surface with the highest elevation above the target is expected to be nearly horizontal on average over a pixel. For such a near-horizontal pixel, the ratio of the observed signal to that of the generic light pattern defined in Section 2 is the same for both LEDs, and it is equal to the ratio  $R_r$  between the reflectance of the collected particle and that of silver black (11 per cent). The modelled profiles for a spherical particle exhibiting Lambert scattering with a uniform reflectance of 11 per cent collected at the mid-point between the two LEDs are shown in Fig. 11.

At the mid-point between the two LEDs (distance: 13 mm), the cosine of the incidence (81.25°) is low (0.154), and for each LED the modelled signal level sharply rises when moving from the top of the particle towards the LED as the local incidence of the imaged surface element decreases down to 0° near the edge of the particle (Fig. 13). When considering the sum of the P and M ratios, there is a minimum of  $\sim 2R_r$  around the crossover point extending over regions with slopes  $< 8.75^\circ$  (one ratio goes down, the other compensates), with a value more than three times lower than that corresponding to the region close to the edge (near normal incidence).

Actual profiles are expected to show lower contrasts due to the limits on spatial resolution (13.9  $\mu\text{m pixel}^{-1}$ ), the spread in incidences (1 mm wide LED output lens) and possible departures from a spherical shape. Nevertheless, the signature of a convex opaque particle for which surface scattering dominates is the presence of a well-defined minimum when plotting the sum of the ratios of the M and P signals to their reference signal level along the M–P direction. Particles situated closer to one of the two LEDs should exhibit asymmetric profiles with a higher maximum ratio for the LED farthest from the particle.

Example profiles of compact and cluster particles (Fig. 12) demonstrate that the assumption that surface scattering dominates needs to be re-examined for all cluster particles as well as for some compact particles. 2CF/Lambert (Fig. 12, top left) is a 100  $\mu\text{m}$  sized

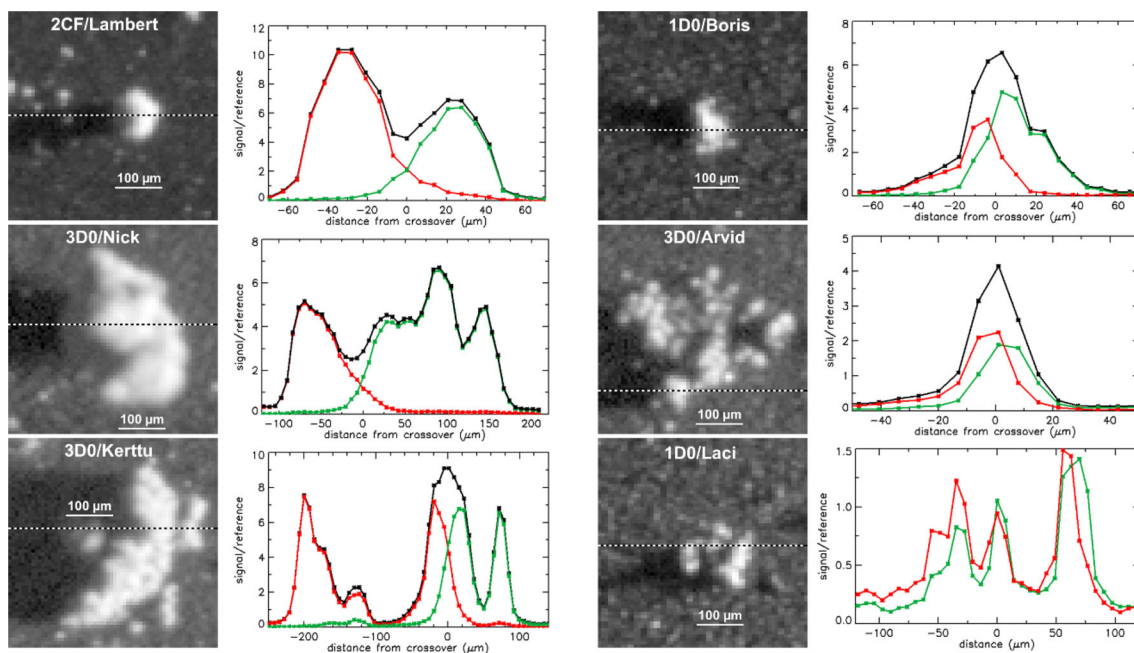


**Figure 12.** Profiles of the ratio of the signal to the reflectance for LED P (green), LED M (red) and the sum of the two ratios (black) for six collected particles with sizes ranging from 100  $\mu\text{m}$  (2CF/Lambert) to 400  $\mu\text{m}$  (3D0/Kerttu) along the dashed line on the image of the particle (left of the profiles, LED P, log scale).

representative of a class of compact particles with a small contact area with the gold black layer. It lies 11.6 mm away from LED P and 14.6 mm away from LED M, which is consistent with the asymmetric profile with a larger maximum of the LED M ratio. There is a well-defined minimum around crossover for the sum of the two ratios. The contrast between the minimum value (near the top of the particle) and that observed for steeper slopes left and right is lower than expected from the model (Fig. 11); hence, an additional contribution (e.g. from scattering within the particle instead of at its surface) may have to be considered, and the estimation of the reflectance from the surface scattering model (4.3 for the sum at crossover/2  $\times$  11 per cent = 24 per cent) is likely to be on the high side.

3D0/Nick (Fig. 12, centre left) is a much larger compact particle (340  $\mu\text{m}$  in size). The minimum at crossover has similar characteristics to that of 2CF/Lambert. The radius of curvature at the crossover is larger than for 2CF/Lambert; hence, a near-horizontal surface element covering more than one pixel is more likely, and the resulting evaluation of the reflectance based on the surface scattering model (2.6 for the sum at crossover/2  $\times$  11 per cent = 14.3 per cent) should be more reliable for 3D0/Nick than for smaller compact particles such as 2CF/Lambert.

3D0/Kerttu (Fig. 12, lower left) is a large compact particle that is highly irregular down to scales of a few 10  $\mu\text{m}$ . While profiles across the lower part of the particle present a weak minimum at crossover, suggesting that surface scattering plays a major role, the profile across the narrowest region of the main component behaves quite differently, with a maximum of the sum of the two ratios at crossover and significant signal from the other LED for the sample exhibiting the peak value of the ratio with one LED. Such a situation cannot be reconciled with the surface scattering assumption: As the peak sample for the LED P profile should then correspond to the minimum mean incidence (hence the maximum mean slope), this sample should be in shadow with the other LED. This indicates that the porosity of 3D0/Kerttu leads to a mean free path larger than a

pixel, so that some photons coming from one side of the particle make their way through the particle to regions facing the other side.

The crossover of the profiles for cluster particles definitely support the view that the scattering of photons is not restricted to a region a few wavelengths thick for this class of particles. 1D0/Boris (Fig. 12, top right), a rubble pile with a similar size as 2CF/Lambert ( $\sim$ 100  $\mu\text{m}$ ) exhibits a maximum of the sum of the two ratio profiles at crossover (instead of a minimum) and maximum values for LED P and LED M which are separated by only one sample interval (6.95  $\mu\text{m}$ ). This overlap becomes even more pronounced when the size decreases from 1D0/Boris to  $\sim$ 40  $\mu\text{m}$  for one of the components of 3D0/Arvid, a shattered cluster (Fig. 12, middle right), with a maximum at the same sample for the P and M ratio profiles resulting in a symmetrical triangular shape for the sum of the two ratio profiles. 1D0/Laci, a shattered cluster smaller than 3D0/Arvid has components 20  $\mu\text{m}$  in size or less, and the P and M profiles become quite similar (Fig. 12 bottom right). The role of porosity within cluster particles (or ‘compact aggregates’ such as 3D0/Kerttu) needs to be better constrained by modelling the reflectance of particles with high porosity.

### 3.2 Simulating the reflectance properties of particles with high porosity

In order to model photon scattering properties of highly porous particles, we adapted a Monte Carlo scattering model developed for Martian aerosols (Vincendon et al. 2007). For each interaction, the single scattering albedo defines the probability that a photon is absorbed. If not, it is scattered according to an isotropic law. A Henyey–Greenstein law with forward/backward scattering lobes has also been tested, but results are not strongly impacted as phase angles are close to 90° for Cosiscope.

The single scattering albedo was set at 0.3, so as to obtain a reflectance factor of  $\sim$ 7 per cent for a semi-infinite medium, in line with the mean reflectance factor of the nucleus at 650 nm at

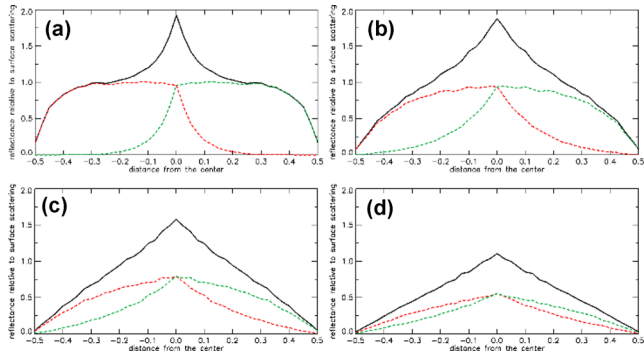


**Figure 13.** Radiance in the  $+z$  direction resulting from the Monte Carlo simulation for the LED P profile (green dashed line), the LED M profile (red dashed line) and the sum of the two profiles (solid line) for a mean free path of 0.1 (a), 0.25 (b), 0.5 (c) and 1 (d) relative to the size of the particle. The simulated particle is positioned half-way between the two LEDs (13 mm distance). The reference for radiance is that resulting from surface scattering (constant incidence of  $36.25^\circ = 45-8.75^\circ$  for the side of the wedge shaped particle facing the LED).

macroscopic scales (Fornasier et al. 2015). The reflectance factor is much lower than the single scattering albedo as most photons undergo several scattering events before escaping the half-space occupied by scattering centres (Wolff et al. 2009).

We selected a triangular wedge shape perpendicular to the X direction (LED M to LED P) with a slope of  $45^\circ$ , which corresponds to elongated rubble piles such as 1D0/Hanna or 3D0/Eloi. The simulation is initiated by distributing scattering centres homogeneously within a volume corresponding to the particle. By modulating the density of scattering centres within the volume, one can control the optical depth for a given reference length within the triangular particle (e.g. its base), which is directly linked to the mean free path. A large number of test photons are then sent from the direction of the LED (P or M). For the sake of simplicity, any test photon hitting the gold substrate in its random walk is considered as absorbed, as 1.8 per cent is very close to 0.

The results of this simplified simulation (Fig. 13) provide important clues on the impact of scattering within the volume of a porous particle on the light profiles. As soon as the mean free path reaches 10 per cent of the size of the particle, there is significant overlap of the P and M profiles near the top of the particle, and the sum of the two profiles reaches a maximum at crossover. For both the P and M profiles, the radiance decreases near the edge closest to the LED as some photons are absorbed by the gold black substrate and it extends beyond the centre as some photons move across the particle. The sum of the two profiles becomes triangular when the mean free path increases with respect to the size and for a mean free path equal to the size of the particle, the two profiles become quite similar. This trend is expected as for large mean free paths, the radiance as seen from above is proportional to the column density of scattering centres in each pixel (a triangle in the simulated case) for both lighting directions. 1D0/Boris (size:  $100\ \mu\text{m}$ ) as well as the components of 3D0/Arvid (size:  $\sim 40\ \mu\text{m}$ ) or 1D0/Laci (size:  $\sim 20\ \mu\text{m}$ ) are not triangular wedges with a  $45^\circ$  slope on both sides, and their porosity may be different. However, the similarity of their respective P, M and summed ratio profiles to that presented in the b, c, d sequence of Fig. 13 (mean free path = 0.25, 0.5, 1 with respect to the size of the particle) shows that the mean free path within cluster particles lies in the 20–25  $\mu\text{m}$  range.

The fraction of photons crossing the particle then reaching the shadowed area remains quite low as long as the mean free path

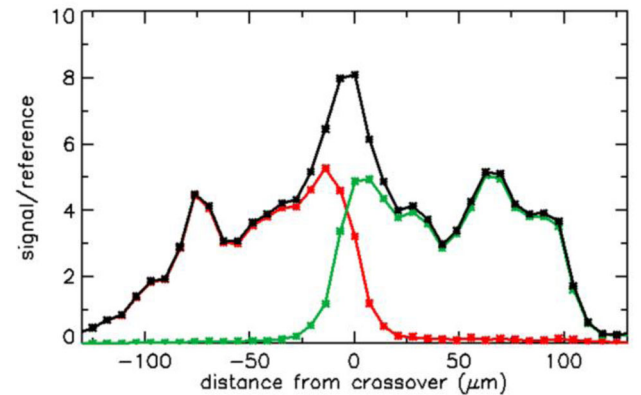
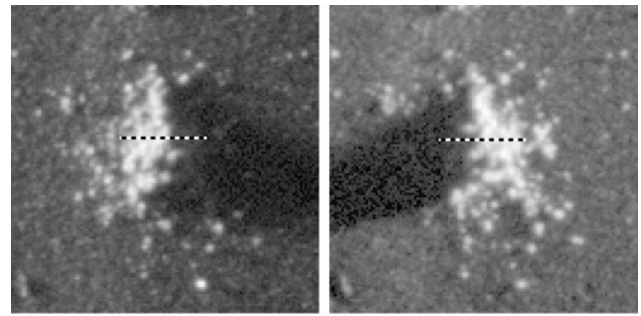


**Figure 14.** Images of 3D0/Eloi with LED M (top left) and LED P (top right) in log scale. The central component of this large rubble pile ( $400 \times 300\ \mu\text{m}$ ) is elongated in the Y direction. The profiles of the normalized signal along the dashed line in the images are displayed in the bottom panel (green: LED P; red: LED M; black: sum of the two LEDs).

does not reach 50 per cent of the size of the particle (the contrast of the shadow is still  $\sim 80$  per cent in that case). This explains why cluster particles (or components for shattered clusters) have very well defined shadows as long as their size is larger than  $50\ \mu\text{m}$ . Other shapes have also been tested, in particular spheres tangent to the target (similar to compact particles). The sum of the two profiles is still maximum near the top, but the match is not as good as with wedge/pyramid shapes, in line with the images which indicate that cluster particles are in contact with the target at their base (Fig. 12, right column) contrary to compact particles (Fig. 12, left column).

The volume containing scattering centres was selected with a wedge shape so as to simulate large rubble pile particles elongated in the Y direction, such as 3D0/Eloi. The actual profiles of 3D0/Eloi (Fig. 16) demonstrate that even such a simple simulation is already representative. Eloi lies at 13.6 mm from both LEDs, with an altitude of  $110\ \mu\text{m}$  and a main component that is  $\sim 200\ \mu\text{m}$  wide at the location of the profiles, so that the mean slope is close to  $45^\circ$ . There is a clear similarity with Fig. 13(a) (mean free path  $\sim 10$  per cent of the size at the base), with a significant signal for each LED more than  $20\ \mu\text{m}$  beyond the crossover, in line with the mean free path set at 10 per cent of the width in the simulation. With such a large ratio between the size and the mean free path, the modelled level of light in the shadow is extremely low (contrast  $> 99.5$  per cent of that of the shadow of an opaque particle), in line with the observed profiles (Fig. 14).

The relationship of the mean free path and the porosity depends on the size of the scattering centres (the smaller the size, the larger the required porosity for a given mean free path) and their distribution in space (there must be some continuity for holding the particle together). If scattering centres are a few  $\mu\text{m}$  in size or less (in line

with observations by MIDAS, the atomic force microscope of *Rosetta*, Bentley et al. 2016), the porosity must be higher than 90 per cent for obtaining a mean free path of 20  $\mu\text{m}$ . In any case, the size of the scattering centres cannot be larger than the mean free path, hence the porosity of large particles (100  $\mu\text{m}$  and more) must be high (>50 per cent) for the mean free path to reach a significant fraction of the particle size.

It is important to note that with mean free paths up to 25 per cent of the size of the particle, the maximum radiance derived from the model (Fig. 12) remains close to that expected from surface scattering, proportional to the cosine of incidence ( $i = 36.25^\circ$  in the simulated case). This means that incidence remains the controlling parameter for radiance even taking into account porosity as long as the particle is at least four times larger than the mean free path (from 100  $\mu\text{m}$  – the size of 1D0/Boris – up). Furthermore, photons coming in at a given location can come out several 10  $\mu\text{m}$  away, which averages out local slopes for irregular cluster particles. This makes it possible to define a method based on the maximum light level which can be applied to both compact particles and cluster particles.

### 3.3 The representative maximum light level as a benchmark for reflectance

As discussed in Langevin et al. (2016) and in the preceding section, large particles have well-defined shadows that make it possible to evaluate their maximum height above the target, one the discriminating criteria between the different types of cluster particles. The height to size ratios range from 0.2 to more than 1 for particles larger than 100  $\mu\text{m}$ , so that the mean slope ranges from  $22^\circ$  to more than  $63^\circ$ . At the mid-point between the two LEDs, the incidence on the target is  $8.75^\circ$ ; hence, the incidence assuming a constant slope facing the LED ranges from  $18^\circ$  to  $59^\circ$ . The maximum slope is at least as large, and in general larger than the mean slope. Rubble piles exhibit significant structure at intermediate scales (see e.g. Fig. 14 for 3D0/Eloi). For shattered clusters, the height/size ratio is larger for individual components than for the particle as a whole. Therefore, the minimum incidence on the side of the particle facing each LED is very likely to be in the range of  $45^\circ$  or less. For compact particles such as 2CF/Lambert or 3D0/Nick (Fig. 12), this minimum incidence is expected to be even lower. Conversely, the 13.9  $\mu\text{m}$  pixel size is not filled out by a near-vertical facet for compact particles close to 100  $\mu\text{m}$  in size, and the scattering of photons within porous particles lowers the radiance from areas close to the base of the particle, which exhibit the largest slopes for pancake-shaped particles such as 2CF/Jessica. Overall, the most likely range of the maximum incidence averaged over a pixel lies between  $25^\circ$  and  $55^\circ$ , with a light level within a factor of 0.82–1.3 compared to that resulting from a  $45^\circ$  incidence. For cluster particles, the minimum incidence is evaluated at  $30^\circ$ , and the relative uncertainty is  $\pm 20$  per cent (factor 0.8–1.2).

The approach that has been selected therefore consists in determining the maximum light level of each particle with each LED, then assuming that this maximum light level corresponds to a  $45^\circ$  incidence. The reference light level for the silver black target at the same location (see Section 2) results from a cosine of the incidence equal to  $2/D_p$  ( $2/D_m$ ), where  $D_p$  ( $D_m$ ) is the distance to LED P (LED M) in mm, which is known. This provides an evaluation of the ‘ $45^\circ$  equivalent reflectance factor’:

$$\text{RF}_{45\text{P}} = \text{maxP}/\text{refP} \times 2/D_p/0.7 \quad (1)$$

$$\text{RF}_{45\text{M}} = \text{maxM}/\text{refM} \times 2/D_m/0.7 \quad (2)$$

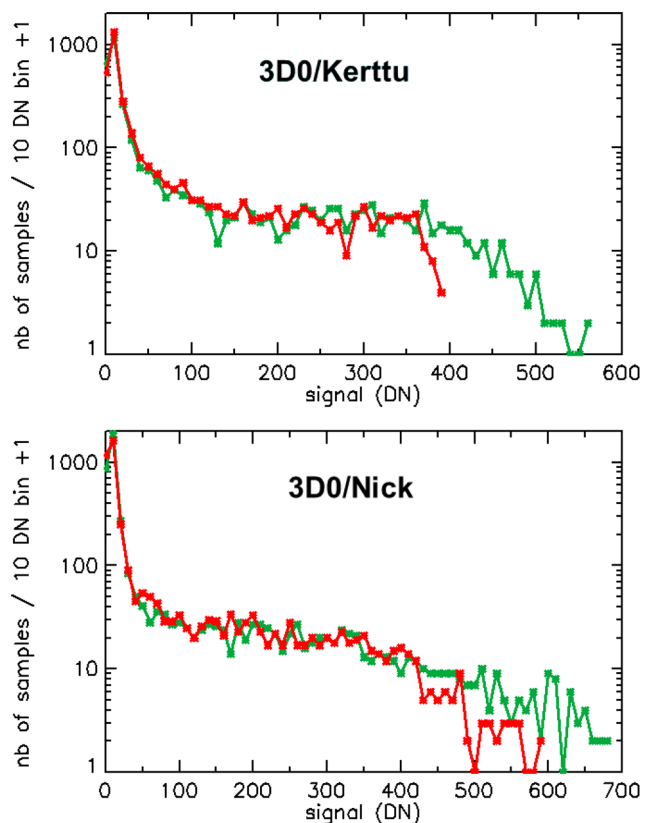


**Figure 15.** Histograms of signal levels for two large compact particles, 3D0/Kerttu (top) and 3D0/Nick (bottom); green: LED P; red: LED M. The histograms are displayed in log scale for clarity, with a value of 1 meaning ‘no samples in the 10 DN bin’.

This approach assumes that the particle has a relatively homogeneous reflectance. Otherwise, the maximum light level corresponds to the maximum of the product of the local reflectance factor and the cosine of the local incidence. In order to be representative of a well-defined local slope with regular (Lambert-like) scattering properties, the maximum value must be the end member of a continuum of sampled values. One therefore needs to check the histograms of DN levels for each LED. For the largest particles, there are up to 1000 distinct samples (with 6.95  $\mu\text{m}$  sampling) that provide a significant statistical basis.

Histograms exhibiting a plateau for intermediate values are a signature of compact particles, as shown in Fig. 15 for 3D0/Kerttu and 3D0/Nick. This behaviour corresponds to that of a single spherical particle, or a combination of spherical segments of any size. When the high end of the histogram shows small gaps, one can be slightly conservative when evaluating the maximum representative light level (3D0/Kerttu: 500 DN for LED P, 380 DN for LED M; 3D0/Nick: 650 DN for LED P, 550 DN for LED M) as isolated values may not be representative.

The histograms of rubble piles are quite different from that of compact particles, as shown in Fig. 16. The frequency of signal levels decreases more rapidly for intermediate values than for histograms of large compact particles. More importantly, there are isolated samples with a signal which can be more than twice larger than the upper limit of the continuous part of the histogram (2D1/Alexandros, Fig. 16, top). Such samples cannot be considered as representative of the upper end of a distribution of local slope/reflectance factor combination.

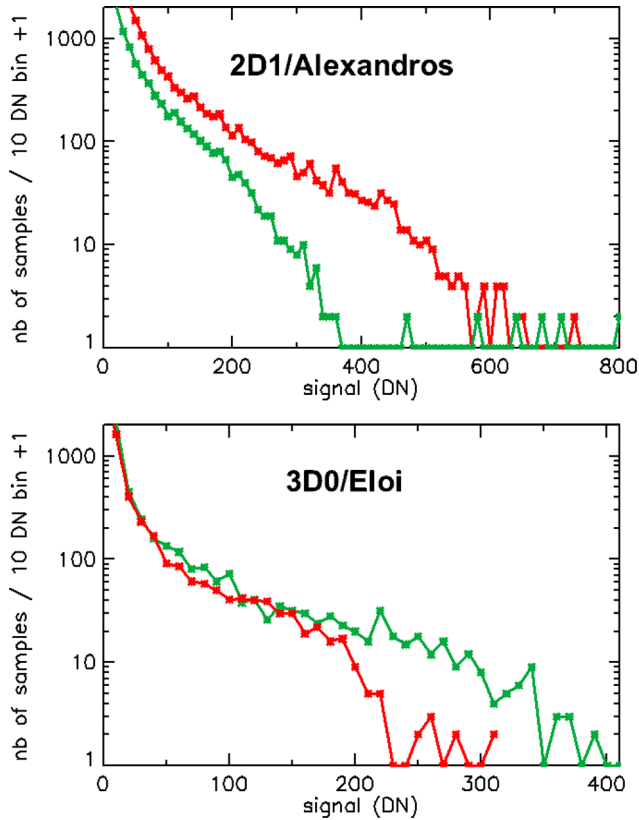


**Figure 16.** Histograms of signal levels for two large rubble piles, 2D1/Alexandros (top) and 3D0/Eloi (bottom); green: LED P; red: LED M. The histograms are displayed in log scale for clarity, with a value of 1 meaning ‘no samples in the 10 DN bin’. The signal level considered as representative of a maximum slope/reflectance factor is 330 DN (LED P) and 550 DN (LED M) for 2D1/Alexandros, 370 DN (LED P) and 220 DN (LED M) for 3D0/Eloi.

The histograms of shattered clusters such as 2CD/Karen and 1CF/Hase exhibit an even steeper decrease for intermediate signal levels (Fig. 17) than rubble piles (Fig. 16). Shattered clusters are constituted of many individual components, so that the relevance of a ‘mean’ slope becomes marginal. The histograms of the signal for shattered clusters often exhibit isolated samples (seven for Karen with LED P, six for Hase with LED M) which cannot be considered as representative of the upper end of a distribution of local slopes (or reflectance factors). For the smallest shattered clusters, such as 1CF/Hase, the statistics become quite poor and one reaches the limits of the approach as it becomes difficult to unambiguously define representative maximum values of the signal.

A combination of large slopes and/or bright patches with an extension of only one or a few samples leading to a contrast of up to a factor 3 compared to neighbouring areas is unlikely. These anomalously high signals are more likely to result from specular reflection on facets of crystalline particles at pixel scales (10–20  $\mu\text{m}$ ). This view is supported by the observation of olivine crystals deposited before launch on one of the flight targets (Fig. 18) as a reference material for mass spectrometry.

The pre-launch dispersion of olivine crystals generated a large artificial shattered cluster, with many components identified in log scale (Figs 18a and b). In linear scale (Figs 18c and b), only a few samples show up quite brightly, most likely due to a specular re-

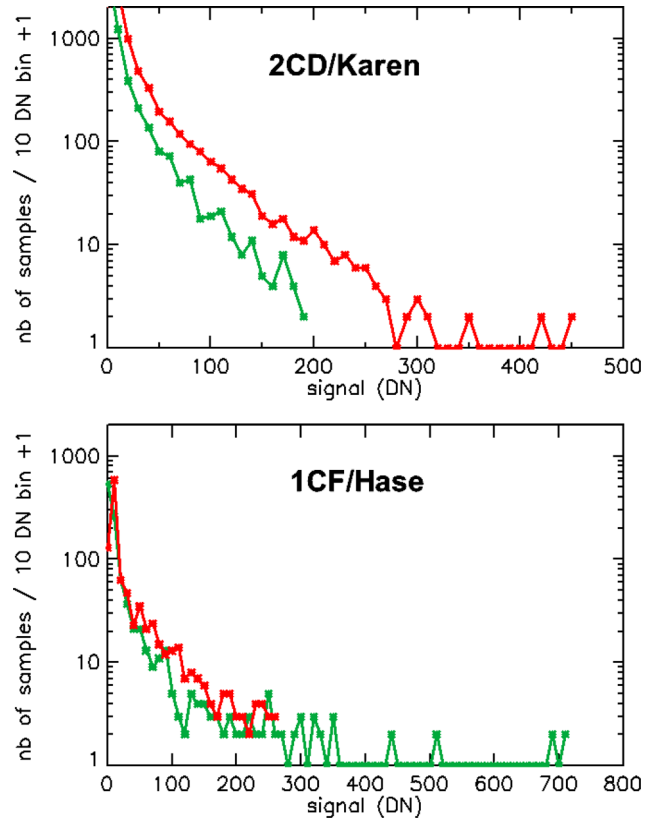


**Figure 17.** Histograms of signal levels for two shattered clusters, 2CD/Karen (top) and 1CF/Hase (bottom); red: LED P; green: LED M. The histograms are displayed in log scale for clarity, with a value of 1 meaning ‘no samples in the bin’. The signal level considered as representative of a maximum slope/reflectance factor is 190 DN (LED P) and 270 DN (LED M) for 2CD/Karen, 300 DN (LED P) and 240 DN (LED M) for 1CF/Hase.

flexion configuration. Isolated values similar to that observed for cometary rubble piles or shattered clusters are identified in the P and M histograms. Therefore, the most likely interpretation of the isolated values observed for cometary particles is that they also correspond to specular reflections on small mineral sub-components. Images of COSIMA particles in linear scale (Fig. 19) support this interpretation. For 2D1/Sylvain, the near continuous area with a lower reflectance factor than the three bright samples corresponds to expectations for the side of a large homogeneous rubble pile facing the LED (P in that case). This validates screening out standalone high signal samples when evaluating the reflectance factor from representative maximum values, as presented in Figs 16 and 17.

Such samples with anomalously high signal levels provide the best evidence from Cosiscope for a contribution of crystalline components to cometary material. More than 70 per cent of cluster particles display anomalous bright samples, which indicate that crystalline components in the size range of the Cosiscope pixels (13.9  $\mu\text{m}$ ) are common. This is in line with observations of crystalline components a few  $\mu\text{m}$  to a few 10  $\mu\text{m}$  in size in interplanetary dust particles collected in the stratosphere of the Earth (Thomas et al. 1995; Messenger et al. 2015). One cannot draw meaningful constraints on the abundance of such crystalline components from the very low proportion of anomalously bright samples (<1 per cent) as it mainly results from the small solid angle of the collecting optical lens as seen from the target (20 mm at a distance

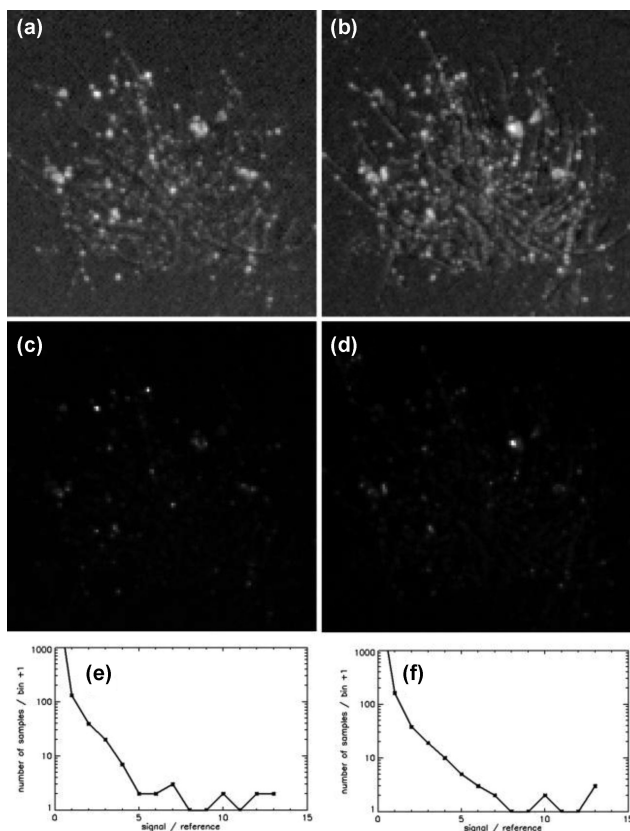


**Figure 18.** Patch of olivine crystals imaged with a log scale (a: LED P; b: LED M) and with a linear scale (c: LED P; d: LED M). Parts (e) and (f) show the histograms of values normalized to the silver black reference for LED P and LED M, respectively.

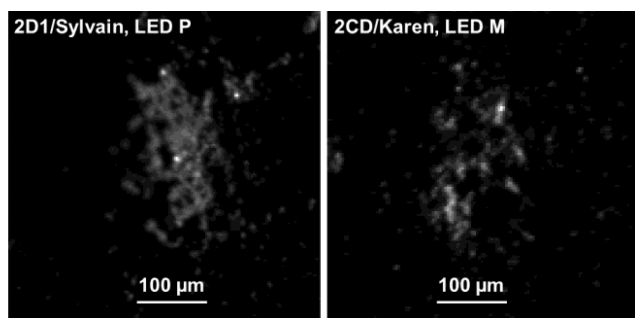


**Figure 19.** Anomalous bright samples on images (linear grey scale) of 2D1/Sylvain (left), a large rubble pile, and 2CD/Karen (right), a large shattered cluster.

of 70 mm), while the non-specular signal from transparent crystalline components is low with grazing incidence, as demonstrated by Fig. 18 for a pre-launch dispersion of olivine crystals.

## 4 OPTICAL PROPERTIES OF COMETARY PARTICLES COLLECTED BY COSIMA

### 4.1 Results for large collected particles, relationship with type, size and time of collection

Best estimates of the reflectance factor of 225 particles were determined from Equations (1) and (2) after screening out anomalously high samples as discussed in Section 3.3, while more than 300 par-

ticles larger than 100 μm. were collected on the 21 exposed targets (7 target assemblies). The light flux reaching particles collected on targets 1C7 and 1C1 (silver blank) is expected to be larger than for other targets due to specular reflection. Applying Equations (1) and (2) on particles collected on these two targets confirmed that the resulting reflectance factors were systematically very high. Evaluating the contribution from specular reflection is far from straightforward, and particles collected on these two targets were not considered. Particles lying in the shadow of a large particle for one of the two LEDs were also excluded, so as to be able to rely for each particle on two independent evaluations from LED P and LED M.

The estimated relative uncertainty on reflectance factor values for cluster particles is  $\pm 20$  per cent. Selecting representative maximum values introduces a bias in favour of brighter areas, with a reflectance factor evaluation that can be overestimated compared to the mean reflectance factor. Equations (1) and (2) also overestimate the reflectance factors of convex compact particles by a factor of up to 1.4 if the incidence is lower than  $15^\circ$  for areas extending over many samples.

There is no significant correlation of the derived reflectance factors with the position on the target (Fig. 20), which indicates that the large variations of the reference light levels, by factors of up to 20 across the target, are correctly evaluated (see Section 2).

The ratio of the P and M reflectance factor is  $1.15 \pm 0.3$  (standard deviation), so that most particles lie close to the 1:1 line, even if there are a few puzzling cases (one particle shows up with a 18 per cent P reflectance factor and a 6 per cent M reflectance factor). This relatively good match between reflectance factors estimated from LED P and LED M images (Fig. 21) supports the reliability of the procedure: On average, particles with a steeper slope and/or higher reflectance factor on their left side or their right side should balance out. The entry funnel has angle of  $\pm 20^\circ$ , so that incoming velocities are close to normal to the target. For cometary particles with low strength (Hornung et al. 2016), a relatively symmetrical rubble pile structure can be expected after impact, which is the case for 3D0/Eloi (Fig. 14). The small bias in favour of the P reflectance factor (10.4 per cent median value instead of 9 per cent median value for the M reflectance factor) could result from a slight tilt of the reference target (3D2) which favoured LED M over LED P when evaluating the generic light levels, as indicated in Section 2.2.3.

The estimated reflectance factors for the two best candidates for the ‘crossover’ approach presented in Section 3.1 are 17.3 per cent (P) and 20.1 per cent (M) for 2CF/Lambert (crossover: 24 per cent), 16.4 per cent (P) and 15.1 per cent (M) for 3D0/Nick (crossover: 14.4 per cent). The two evaluations are relatively close given the question marks on the surface scattering hypothesis: For 2CD/Lambert, which is much smaller than 3D0/Nick, some photons observed coming out of the top may have entered the particle at a higher incidence, explaining the higher value with the surface scattering assumption.

The reflectance factors of compact particles (Fig. 22, top left) are on average 1.5 times larger than for cluster particles. While a difference in composition of compact particles cannot be ruled out, the higher reflectance factor could also be in part due to the larger slopes (hence smaller incidences) of compact particles compared to cluster particles. An element that supports the view that many compact particles could be constituted of the same material as cluster particles with a more cohesive packaging is provided by the disaggregation of many compact particles into rubble piles after ion analysis. This supports a low cohesive strength that could be overcome by electrostatic forces under the ion gun. The reflectance factor after the

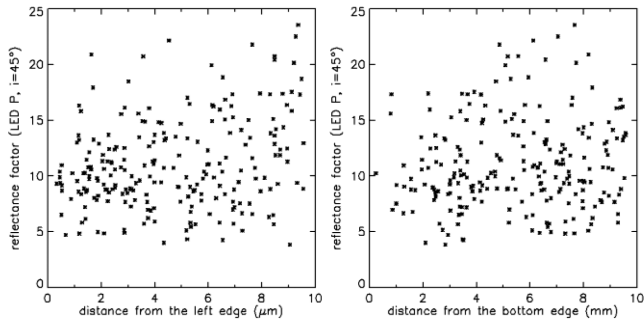


**Figure 20.** Reflectance factor derived from signal levels with LED P with the  $45^\circ$  incidence assumption as a function of the position on the target along the X axis (top) and the Y axis (bottom).

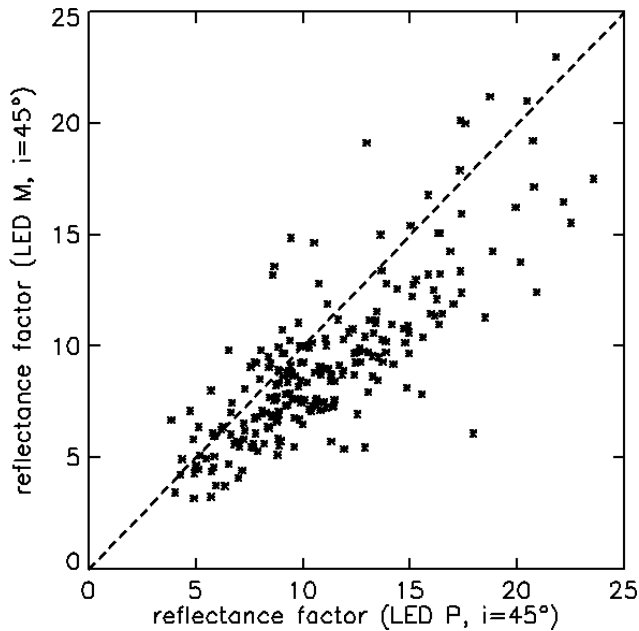


**Figure 21.** Reflectance factors of all 225 particles as derived from signal levels with LED P and LED M.

transformation is lower by a factor of 2 for 1D0/Andrzej (from 23 per cent to 11.5 per cent) and by a factor of 1.4 for 3D0/Kertttu (from 21 per cent to 14 per cent), which can to a large extent be interpreted as resulting from a larger minimum incidence.

As discussed in Merouane et al. (2016), the evolution with time is a complex issue as several controlling parameters (distance to the Sun, distance to the comet, local time, ram direction) are changing simultaneously. Within these limitations, the evolution of reflectance factor with time seems to be relatively minor. Fig. 22 points towards a dearth of particles with reflectance factors larger than 15 per cent after perihelion. This is confirmed when considering the collection date of each particle relative to perihelion (Fig. 23): after perihelion, only one large particle with an average reflectance factor larger than 15 per cent was collected.

This restricted range of reflectance factors post-perihelion results mainly from the absence of large compact particles ( $>100 \mu\text{m}$ ) in this time range, as they constitute a major contribution for reflectance factors larger than 15 per cent. A higher mass-loss rate of 67P/Churyumov–Gerasimenko before perihelion was inferred by Moreno et al. (2004) from ground observations.

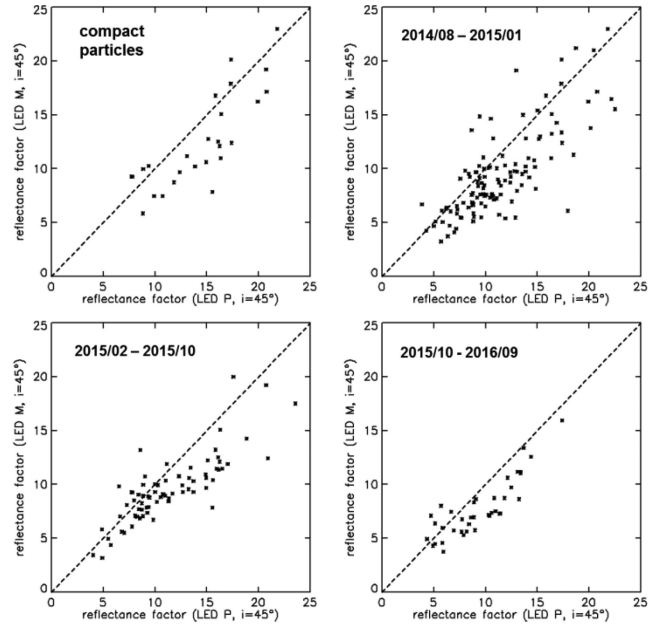


**Figure 22.** P and M reflectance factors for compact particles (top left) and for all particles in three time intervals: pre-perihelion (2014 August to 2015 January, top right), around perihelion (2015 February to 2015 October, bottom left) and after perihelion (2015 October to 2016 September, bottom right).

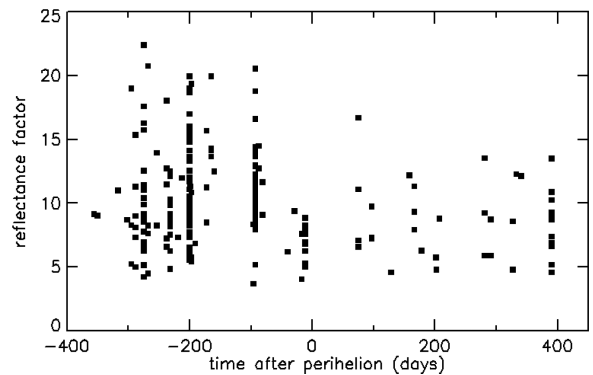


**Figure 23.** Average reflectance factor  $(P+M)/2$  as a function of the collection time relative to perihelion.

The relationship between size and reflectance factor is presented in Fig. 24. There is no obvious trend except for a larger proportion of dark particles (reflectance factor  $<7$  per cent) in the smaller size range ( $<150 \mu\text{m}$ ). One possible interpretation is that dark, carbonaceous-rich particles could have a lower tensile strength than brighter particles, resulting in smaller fragments. As one selects the brightest representative sample in the images of a particle (see Section 3), both the relationship of variegation with size and absorption by the underlying gold black substrate for particles thinner than the mean free path should have a limited impact. Small sub-components of shattered clusters (e.g. 1D0/Lacy, Fig. 12) could result in lower light levels as a fraction of photons escape the particle in the forward direction.

As discussed in Merouane et al. (2016) and Langevin et al. (2016), there are prominent peaks in the collection rate, in particular, but not only, far from the comet. This has been associated with two different processes:

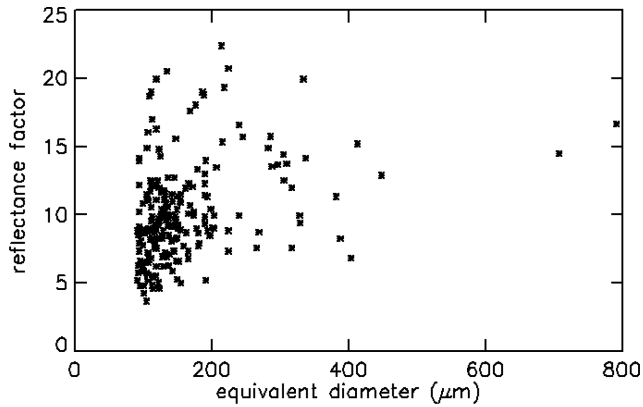


**Figure 24.** Relationship between the diameter of a disk with the same area as each particle and its average reflectance factor  $(P + M)/2$ .

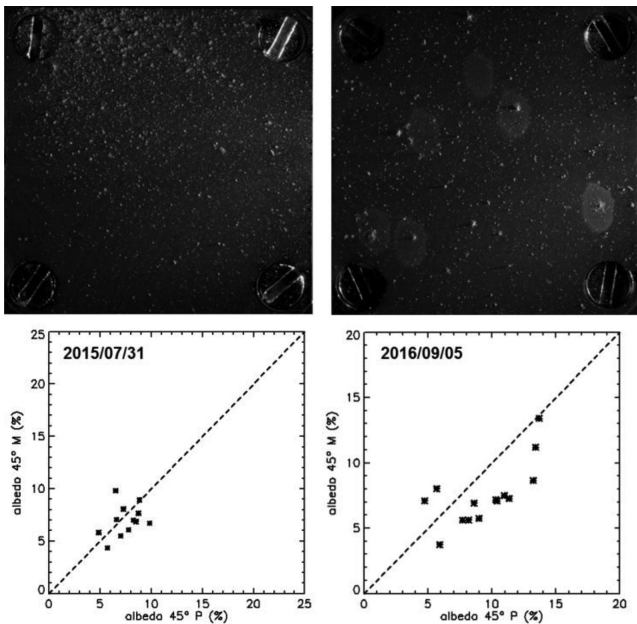


**Figure 25.** Spatial distribution (top) and estimates of reflectance factors (bottom) for two large collection events, one near perihelion (2015 July 31, left), the other close to the end of the mission (2016 September 05, right).

- Outbursts (observed by OSIRIS and the navigation cameras) can result in a transient increase of the particle density near the comet.

- Far from the comet, major collection events are attributed to the breakup of large parent particles in the entry funnel of COSIMA.

The evaluation of reflectance factors and spatial distributions support this view: as demonstrated by Fig. 25, a period of less than 1 d (2015 July 31) close to perihelion resulted in many collections on target 2D1, with a strong enhancement near the top left corner. Particles are so close together in that region that mutual shadowing is prevalent. The reflectance factors of standalone particles from this collection event are tightly grouped in the 5–10 per cent range. This supports the view that the collected particles result from the disruption of a single dark parent particle. The situation for a collection event close to the end of the mission (2016 September 05) when *Rosetta* was much closer to the nucleus is markedly different: particles are distributed evenly on target 1C3, there are also collected particles on the two other exposed targets, 2C3 and 3C3, and the

range of reflectance factors is much wider. This time interval corresponds to a prominent outburst, and the collected particles were most likely collected individually after being released simultaneously by the outburst. Large collection events earlier in the mission could be associated with one of these two patterns, pointing towards a breakup or outburst origin.

#### 4.2 Comparison with the properties of cometary particles as derived from other *Rosetta* instruments, ground-based observations and analogue extraterrestrial materials

The high porosity required for obtaining mean free paths of 20–25  $\mu\text{m}$  within particles is in line with evaluations of porosity in the 70 per cent range from strength evaluations (Hornung et al. 2016), and the 87 per cent porosity derived for the surface material of the nucleus by OSIRIS (Fornasier et al. 2015). Observations by the atomic force microscope of *Rosetta*, MIDAS, indicate that particles exhibit a complex substructure down to the  $\mu\text{m}$  scale (Bentley et al. 2016) and even at sub- $\mu\text{m}$  scales (Mannel et al. 2016), with a fractal dimension of 1.7 which requires a high porosity. Modelling of polarization results from ground-based observations also lead to very high porosities (84–97.5 per cent, Lasue et al. 2009) in the  $\mu\text{m}$  range. High porosity has been reported at such scales for chondritic micrometeorites (Noguchi et al. 2015). Images of the cavity in which Philae finally got stuck obtained by CIVA (Bibring et al. 2015) and ROLIS (Mottola et al. 2015) exhibit a complex relief in the range of a few mm to several m. Therefore, the high complexity/porosity observed by Cosiscope in the 10–100  $\mu\text{m}$  range provides one of the elements of a sequence of evidence pointing towards a fractal structuration from the  $\mu\text{m}$  scale to the macroscopic scale. The very high porosity and low-density particles ( $\sim 1 \text{ kg m}^{-3}$ ) inferred from GIADA observations (Fulle et al. 2015) are not observed by Cosiscope, as they would not project well-defined shadows. Such very weak particles are expected to break up into very small fragments upon collection even at  $\text{m s}^{-1}$  velocities.

The range of reflectance factors obtained for COSIMA particles (3–23.5 per cent for both LED P and LED M) is broader than that observed at 650 nm at regional scales by OSIRIS (6–8 per cent, Fornasier et al. 2015) and the median reflectance factor value obtained by Cosiscope ( $\sim 10$  per cent at 640 nm) is higher than that of the brightest regions at these scales. This could be expected as the selection of the brightest representative sample for each particle, leading to Equations (1) and (2), is likely to lead to values higher than the mean reflectance of a particle. It should also be mentioned that hierarchical accretion implies a fractal porosity/roughness model. The number of scattering events could increase with the scale, leading to a decrease of the apparent reflectance factor. There is also more variability at sub-metre scales with OSIRIS (El-Maarry et al. 2015) than at regional scales (Fornasier et al. 2015).

The characterization of cometary dust on the basis of ground observations is a complex issue (see e.g. Kolokolova et al. 2004; Lvasseur-Regourd et al. 2007). The scale over which properties are determined is much larger (up to 10 000 km) than that investigated by *Rosetta*, while albedo has been observed to increase with distance (Hammel et al. 1987). The best observation opportunities are provided by bright long period comets such as C1995/01 Hale-Bopp, which are not representative of Jupiter family comets such as 67P/Churyumov–Gerasimenko. It should however be noted that photometric, polarimetric and spectrometric approaches (e.g. Fulle et al. 1998; Moreno et al. 2003; Lasue et al. 2009) show that cometary particles have irregular shapes, in line with Cosiscope observations, and that a diversity of components is

required, from dark particles mainly constituted of organic material to mineral particles.

The available information on the reflectance factor of chondritic IDPs collected in the stratosphere is close to the Cosiscope evaluations, with ranges of 3–20 per cent obtained by Bradley et al. (1996) and Thomas et al. (1995). The scale is not the same, as the analysed components in IDPs are a few  $\mu\text{m}$  in size while Cosiscope particles range from a few 10 to 800  $\mu\text{m}$  in size. Bradley et al. (1996) also report on a component with more than 90 per cent carbon and a reflectance factor of 12 per cent at 640 nm. Therefore, the range of reflectance factors observed by Cosiscope can be reconciled with a composition dominated by C, H, O and N (Kissel et al. 1986), possibly constituting complex organic compounds (Frey et al. 2016). The bright anomalous samples in the Cosiscope images have been attributed to crystalline sub-components, which are well documented in micrometeorites and IDPs (e.g. Messenger et al. 2015).

## 5 CONCLUSION

Cosiscope, the microscope of COSIMA, implemented grazing incidence illumination of targets by LEDs (wavelength: 640 nm) so as to maximize the probability of detection of particles sticking out of smooth targets. This represented a major challenge for extracting photometric information from the images obtained by Cosiscope. A detailed analysis of the different contributions to the signal made it possible to evaluate the light distribution on smooth targets ('silver black' and 'gold black'). Silver black, with its high signal levels, provides an adequate reference for reflectance, measured at 11 per cent in the laboratory.

From the distribution of the signal within large particles ( $> 100 \mu\text{m}$  in size) compared with a Monte Carlo radiometric transfer model, we have shown that all cluster particles and some apparently compact particles exhibit high porosity, with a best estimate of 20–25  $\mu\text{m}$  for the mean free path of photons within the particle. This scale of porosity contributes to a sequence extending from the  $\mu\text{m}$  scale (MIDAS, ground-based observations, analogue extraterrestrial material) to the macroscopic scale (CIVA/ROLIS, then OSIRIS). Such a mean free path is significant compared to the size of the particles. It smooths out local incidences, and reflectance properties of irregular cluster particles can be constrained from the histogram of signal values within the particle with each of the two LEDs.

Many cluster particles exhibit anomalous bright samples that are interpreted as resulting from specular reflections on crystalline facets in the 5–15  $\mu\text{m}$  size range from the observation of a similar behaviour with a dispersion of olivine particles on one of the flight targets before departure. The common occurrence of crystalline components in this size range in cometary particles is in line with observations of extraterrestrial material.

The best estimates of reflectance factors from the maximum representative signal level range from 3 per cent to 23 per cent. Mean reflectance factors could be lower if there is significant variability within the particles. The evaluations with both LEDs are compatible within uncertainties and taking into account possible asymmetric particle profiles. The reflectance factor range is compatible with macroscopic observations of the nucleus (6–8 per cent at 650 nm) and with photometric studies of interplanetary dust particles collected in the stratosphere of the Earth.

Compact particles are significantly brighter (factor 1.5) than cluster particles. This could be due in part to steeper slopes (hence lower incidences) for the regions exhibiting the largest signal; hence, compact particles could have a similar composition to cluster particles with a tighter packaging. This view is supported by the evolution

of many compact particles under the ion gun, crumbling down as cluster particles.

The only major evolution observed during the orbital phase is the dearth of large compact particles after perihelion, which results in a restricted range of reflectance factor in this time period. Major collection events far from the nucleus can be attributed to the breakup of a single large parent particle as the range of reflectance factors for collected particles is small, consistent with a common constituting material. Major collection events close to the nucleus exhibit a much wider range of reflectance factors, consistent with the simultaneous release of a large number of variegated particles by an outburst.

## ACKNOWLEDGEMENTS

COSIMA was built by a consortium led by the Max-Planck-Institut für Extraterrestrische Physik, Garching, Germany in collaboration with Laboratoire de Physique et Chimie de l'Environnement et de l'Espace, Orléans, France, Institut d'Astrophysique Spatiale, CNRS/Université Paris Sud, Orsay, France, Finnish Meteorological Institute, Helsinki, Finland, Universität Wuppertal, Wuppertal, Germany, von Hoerner und Sulger GmbH, Schwetzingen, Germany, Universität der Bundeswehr, Neubiberg, Germany, Institut für Physik, Forschungszentrum Seibersdorf, Seibersdorf, Austria, Space Research Institute, Austrian Academy of Sciences, Graz, Austria and is led by the Max-Planck-Institut für Sonnensystemforschung, Göttingen, Germany. The support of the national funding agencies of Germany (DLR, grant 50QP 1302), France (CNES), Austria, Finland and the ESA Technical Directorate is gratefully acknowledged. We thank the Rosetta Science Ground Segment at ESAC, the Rosetta Mission Operations Centre at ESOC and the Rosetta Project at ESTEC for their outstanding work enabling the Science return of the Rosetta Mission. *Rosetta* is an ESA mission with contributions from its member states and NASA. *Rosetta's* Philae lander is provided by a consortium led by DLR, MPS, CNES and ASI.

## REFERENCES

- Bentley M. S. et al., 2016, *Nature*, 537, 73  
 Bibring J.-P. et al., 2015, *Science*, 349, aab0671  
 Bradley J. P., Keller L. P., Brownlee D. E., Thomas K. L., 1996, *Meteorit. Planet. Sci.*, 31, 394  
 El-Maarry M. R. et al., 2015, *A&A*, 583, A26  
 Fulle M., Barbieri C., Cremonese G., 1998, *A&A*, 201, 362  
 Fulle M. et al., 2010, *A&A*, 522, A63  
 Fulle M. et al., 2015, *ApJ*, 802, L12  
 Fornasier S. et al., 2015, *A&A*, 583, A30  
 Fray N. et al., 2016, *Nature*, 538, 72  
 Kissel J. et al., 1986, *Nature*, 321, 336  
 Kissel J. et al., 2007, *Space Sci. Rev.*, 128, 823  
 Kolokolova L., Hanner M. S., Levasseur-Regourd A. C., Bustafson B. A. S., 2004, in Festou M. C., Keller H. U., Weaver H. A., eds, *Comets 2*. Univ. Arizona Press, Tucson, AZ, p. 577  
 Hammel H. B., Telesco C. M., Campins H., Decher R., Storrs A. D., Cruikshank D. P., 1987, *A&A*, 187, 665.  
 Hilchenbach M. et al., 2016, *ApJ*, 816, L32  
 Hornung K. et al., 2014, *Planet. Space Sci.*, 103, 319  
 Hornung K. et al., 2016, *Planet. Space Sci.*, 133, 63  
 Langevin Y. et al., 2016, *Icarus*, 271, 76  
 Lasue J., Levasseur-Regourd A. C., Hadamcik E., Alcouffe G., 2009, *Icarus*, 199, 129  
 Levasseur-Regourd A. C., Mukai T., Lasue J., Okada Y., 2007, *Planet. Space Sci.*, 55, 1010

- Mannel T., Bentley M. S., Schmied R., Jeszenszky H., Levasseur-Regourd A. C., Romstedt J., Torkar K., 2016, *MNRAS*, 462, S304
- Merouane S. et al., 2016, *A&A*, 596, A87
- Messenger S. et al., 2015, *Meteorit. Planet. Sci.*, 50, 5365
- Moreno F., Muñoz O., Vilaplana R., Molina A., 2003, *ApJ*, 595, 522
- Moreno F., Lara L. M., Muñoz O., López-Moreno J. J., Molina A., 2004, *ApJ*, 613, 1263
- Mottola S. et al., 2015, *Science*, 349, aab0232
- Noguchi T et al., 2015, *EPSL*, 410, 1
- Thomas K. L. et al., 1995, *Geochim. Cosmochim. Acta*, 59, 2797
- Rotundi A. et al., 2015, *Science*, 347, 3905
- Vincendon M., Langevin Y., Poulet F., Bibring J.-P., Gondet B., 2007, *J. Geophys. Res.*, 112, E08S13
- Wolff M. J., Smith M. D., Clancy R. T., Arvidson R., Kahre M., Seelos F., Murchie S., Savijärvi H., 2009, *J. Geophys. Res.*, 114, CiteID E00D04

This paper has been typeset from a Microsoft Word file prepared by the author.